J Mater Sci (2015) 50:1500–1512
DOI 10.1007/s10853-014-8711-4

Protective enamel coating for n- and p-type skutterudite thermoelectric materials

Young-Sam Park · Travis Thompson · Yunsung Kim · James R. Salvador · Jeffrey S. Sakamoto

Received: 8 September 2014 / Accepted: 6 November 2014 / Published online: 15 November 2014

Abstract Transitioning skutterudite (SKD) thermoelectric technology from space to terrestrial power generation requires oxidation suppression technology. One approach involves the development of protective coatings consisting of the following properties: (i) low thermal conductivity to prevent parasitic heat loss, (ii) low electrical conductivity to prevent short-circuiting, (iii) coefficient(s) of thermal expansion matching that of the thermoelectric material, and (iv) adequate thermal stability and mechanical strength for durability. In this work, n-type $Ba_{0.05}Yb_{0.025}CoSb_3$ and p-type $Ce_{0.9}Co_{0.5}Fe_{3.5}Sb_{12}$ were coated with a silica-based enamel to prevent their oxidation. This work demonstrates the efficacy of enamel coatings for suppressing oxidation of n-type SKD, and for the first time, p-type SKD in static and thermal cyclic heating tests up to 600 °C in air. The coating process, physical characterization of the enamel, and materials characterization data are presented and discussed.

Y.-S. Park · T. Thompson · Y. Kim · J. S. Sakamoto (✉)
Department of Chemical Engineering and Materials Science, Michigan State University, East Lansing, MI 48824, USA
e-mail: jsakamot@msu.edu

Y.-S. Park
e-mail: s_yspark@etri.re.kr

T. Thompson
e-mail: trthompson378@gmail.com

Y. Kim
e-mail: ummelong@gmail.com

Y.-S. Park
Electronics and Telecommunications Research Institute, Daejeon 305-700, South Korea

J. R. Salvador
GM Global Research & Development, Warren, MI 48090, USA
e-mail: james.salvador@gm.com

Introduction

Recent advancements in thermoelectric materials research have created new opportunities for thermoelectric power generation and cooling. These advances may enable higher efficiency terrestrial waste heat recovery [1–3] and space thermoelectric power generation technologies [4, 5]. However, with the exception of radioisotope thermoelectric generators (RTG), use of terrestrial thermoelectric power generation technology has been limited. Radioisotope thermoelectric generators use a radioisotope heat source to generate >500 °C thermal gradients that are sustained for multiple decades [1–3]. Additionally, RTGs operate in vacuum, thus oxidation of the high temperature components does not occur. In terrestrial waste heat recovery, particularly when coupled to internal combustion engines, exposure to elevated temperatures (up to 600 °C) in the presence of air will likely cause oxidation [6–9]. Similarly, the degree of oxidation will depend on the TE materials' compositions.

Skutterudites (SKDs) are promising thermoelectric materials, because they have a relatively high ZT of >1.0 [1–6] and are amenable to machining and metallization [7]. For example, Shi et al. [6] have shown that multiple filled n-type SKD has a ZT of 1.7 at 580 °C. Similarly, Tang et al. [10] have demonstrated that InSb-doped n-type SKD has a ZT of 1.4 near the same temperature. Additionally, Rogl et al. [11] recently reported a ZT > 1.0 for Misch-metal filled p-type SKD at temperatures above 500 °C. However, while SKD-based materials show promise, they are susceptible to oxidation or sublimation, leading to

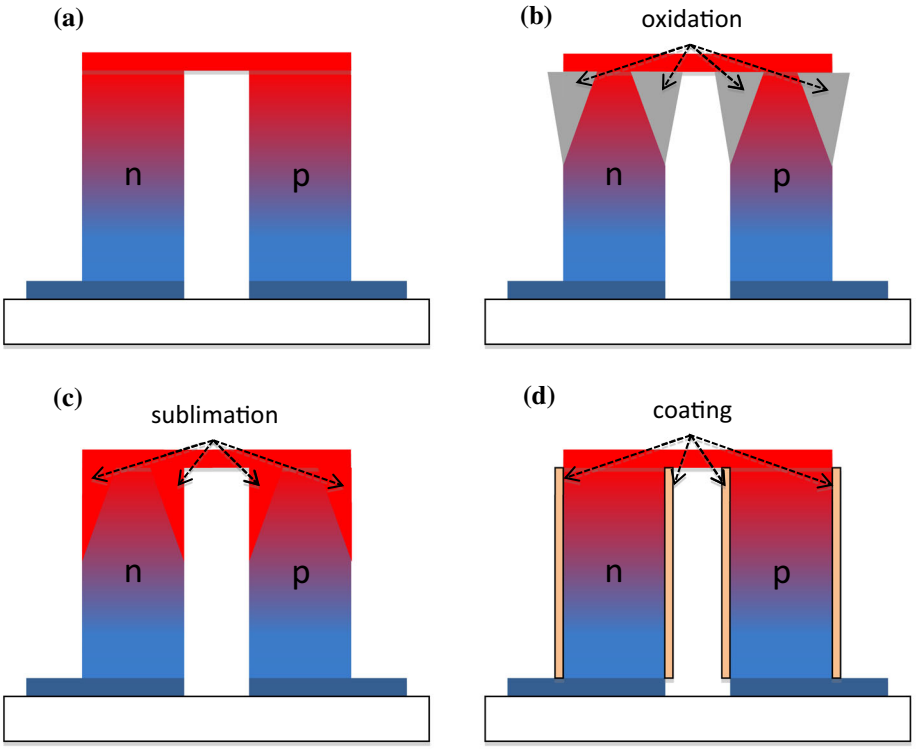

Fig. 1 A schematic diagram showing how degradation can occur in a typical n- and p-power generation couple

performance degradation during operation. A schematic diagram (Fig. 1) shows how degradation can occur in an n/p power generation couple. A typical couple consists of n- and p-type legs connected on the hot side with an interconnect (Fig. 1a). Heating a couple, consisting of air sensitive n- and p-type legs, in air results in oxidation (Fig. 1b). It has been shown that the rapid degradation of thermoelectric modules consisting of n-type $Yb_xCo_4Sb_{12}$ and p-type $Ce_xCoFe_3Sb_{12}$ was due to oxidation from testing in air [12]. While heating a couple in an inert atmosphere can prevent oxidation, sublimation of species such as Sb from SKD [3, 7] also causes couple performance degradation (Fig. 1c). A protective coating could prevent both oxidation and sublimation (Fig. 1d). Promising coating materials include enamel [13], composite glass [14] and aerogel [8, 15]. It has been reported that an enamel coating on n-type $CoSb_3$ is effective in suppressing oxidation up to 600 °C [13]. Similarly, a composite glass coating on n-type $Yb_{0.3}Co_4Sb_{12}$ at 550 and 650 °C has also been demonstrated [14]. However, there have been no reports demonstrating oxidation suppression of p-type SKD. We believe that oxidation of p-type is considerably more challenging compared to n-type SKD owing to the higher weight fraction of oxygen-sensitive-elements such as Ce, Fe, and La. It follows that the purpose of this work was to demonstrate the efficacy of enamel-based oxidation suppression coatings with a specific focus on characterizing oxidation suppression in p-type SKD. The enamel was

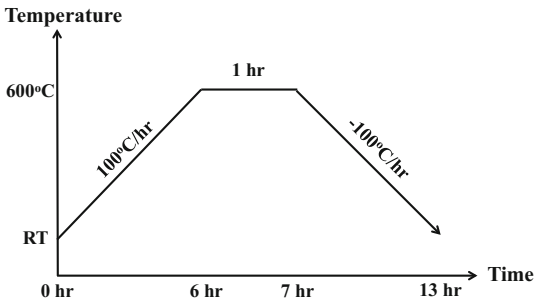

Fig. 2 Thermal cycling time–temperature profile

selected based on its glass transition temperature and flowability to make an airtight seal around SKD elements. Additionally, the enamel has a relatively low thermal conductivity to minimize parasitic heat loss during operation.

We investigated the oxidation suppression behavior and reactivity between the enamel and SKD for both n- and p-type at 500 and 600 °C and subsequently thermally cycled between 600 °C and room temperature. Scanning electron microscopy (SEM), energy dispersive spectroscopy (EDS) and optical microscopy (OM) were used to characterize changes of microstructures or composition before and after heating in air and to compare uncoated and enamel-coated SKD samples. These data along with the enamel processing conditions will be discussed.

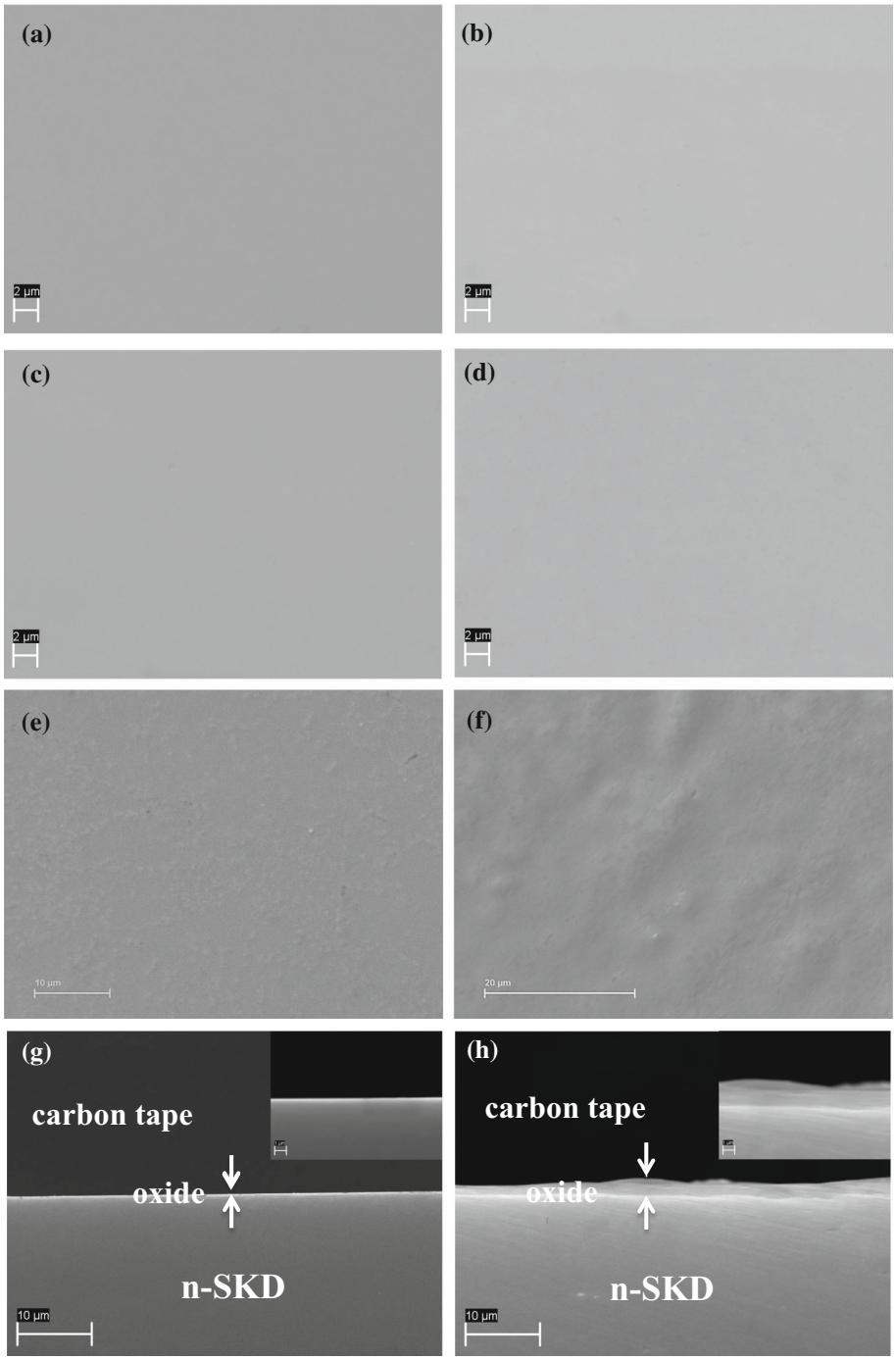

Fig. 3 SEM analysis of n-type $Ba_{0.05}Yb_{0.025}CoSb_3$ after 1 h in air. **a** RT, *top-view*, **b** 100 °C, *top-view*, **c** 200 °C, *top-view*, **d** 300 °C, *top-view*, **e** 400 °C, *top-view*, **f** 500 °C, *top-view*, **g** 400 °C, *vertical-view*, and **h** 500 °C, *vertical-view*

Materials and methods

The n-type $Ba_{0.05}Yb_{0.025}CoSb_3$ and p-type $Ce_{0.9}Co_{0.5}Fe_{3.5}Sb_{12}$ were prepared by a conventional melt, quench, and anneal process [8]. All pure elements were purchased from Alfa Aesar: Sb ingot (99.9 %), Co powder (99.9 %), Fe powder (99.999 %), Ba pieces (99.9 %), Ce pieces (99.9 %), Yb pieces (99.9 %). 100–300 g ingots were pulverized with an automated mortar and pestle, followed by planetary ball milling to further refine the particle size. The powder was loaded into 50 mm diameter graphite dies and hot pressed at 650 °C and 40 MPa pressure under flowing argon. After hot pressing, the pellets were diced into 3.5 × 7.0 × 6.0 mm parallelepipeds using a diamond saw.

Using a tube furnace (Lindberg Blue M), n-type ($Ba_{0.05}Yb_{0.025}CoSb_3$) and p-type ($Ce_{0.9}Co_{0.5}Fe_{3.5}Sb_{12}$) SKD samples were heated to 100, 200, 300, 400, and

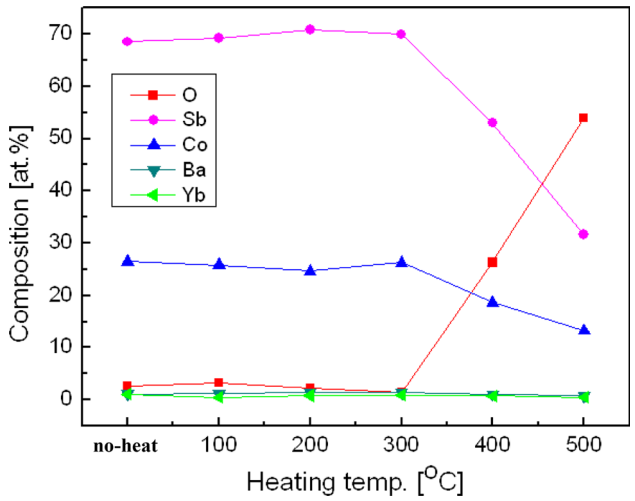

Fig. 4 The element composition change of n-type $Ba_{0.05}Yb_{0.025}CoSb_3$ after 1 h in air heated at up to 500 °C

500 °C in air at a rate of 100 °C/hour. The samples were maintained at each temperature for 1 h, and cooled to room temperature at a rate of 100 °C/hour. An alumina tube with 1.9 cm inner diameter and 60 cm long (CoorsTek Inc.) was utilized to obtain a uniform temperature distribution of the sample in the tube furnace. A silica-based enamel was used in powder form primarily consisting of silicon and sodium oxide (66at.% oxygen, 11at.% silicon, 11at.% sodium, 6at.% fluorine, 2at.% aluminum, 2at.% nitrogen, 1at.% barium, and 1at.% calcium). The enamel powder size ranged from 0.1 to 1.0 μm. To characterize the melting and flowing behavior, enamel powder was melted on copper samples. Cu samples were placed in a crucible, covered with enamel powder and heated to 650 and 700 °C for 1 h in argon gas.

To coat SKD elements with the enamel, the SKD samples were placed in a graphite crucible and then covered in enamel powder. The sample, enamel powder, and crucible were placed in a furnace (MTI KSL-1100X-S), which was housed in an argon filled glovebox, and then heated to 700 °C for 1 h. The oxygen content in the glovebox was maintained at less than 0.3 ppm. To reduce stress and its effects due to orthogonal edges, SKD samples were chamfered manually using 240 grit sanding paper. The approximate chamfer radius was 0.5 mm. After enamel coating, the samples were heated in air at 500 °C for 1 h. Extended (8 days) isothermal air-stability tests were conducted at 500 and 600 °C, respectively. Thermal cycling tests were also conducted and consisting of 20 cycles, where one cycle entailed heating from room temperature to 600 °C at a rate of 100 °C/hour, holding at 600 °C for 1 h, and then cooling to room temperature at a rate of 100 °C/hour (Fig. 2).

Table 1 Oxidation behavior of n- and p-SKD after heating for 1 h in air

T (°C)	n-Type $Ba_{0.05}Yb_{0.025}CoSb_3$	p-Type $Ce_{0.9}Co_{0.5}Fe_{3.5}Sb_{12}$
100	Not measureable	0.1 μm oxide
200	Not measureable	0.4 μm oxide
300	Not measureable	0.8 μm oxide
400	0.1 μm oxide	Spallation
500	1.8 μm oxide	Spallation

Microstructural analysis was conducted using OM (LEICA EZ4D) then SEM (ZEISS EVO LS25). The atomic percent composition was measured using EDS analysis. For EDS analysis, standardless analysis using the library standards provided by the EDS software vendor was used. The software was TEAM (Texture and Elemental Analytical Microscopy) version 3.2. To identify the antimony oxide phase, X-ray diffraction (XRD) measurements were conducted using a Bruker D8 DaVinci diffractometer equipped with Cu-Kα X-ray radiation operating at 40 kV and 40 mA. Laser flash was used to measure the enamel thermal conductivity according to the relationship:

$$\kappa = D \cdot \rho \cdot C_p, \quad (1)$$

where κ is thermal conductivity, D is the thermal diffusivity, ρ is the density, and C_p is the isobaric heat capacity. Thermal diffusivity was measured using a Netzsch (LFA447, laser flash system) up to 250 °C. To obtain the room temperature density, the geometric volume and mass of the test specimen were measured. The heat capacity was measured using a DSC (TA Instruments, Q2000) with a temperature interval of 50 °C. The linear coefficient of thermal expansion (CTE) was measured using a thermal mechanical analyzer (TA Instruments, Q400).

Results and discussion

n-SKD stability versus temperature analysis

The n-type SKD surface topography and composition were analyzed as a function of heating temperature (Figs. 3 and 4). The n-type SKD surface appeared relatively featureless for the control sample, which was not heated (henceforth referred to as RT), and samples heated at 100, 200, and 300 °C (Fig. 3a–d). Above 300 °C, distinct topographic feature changes were apparent (Fig. 3e–f). At 400 °C, 1–2 micron features were observed, likely consisting of antimony oxide as described in more detail below (Fig. 3e). At 500 °C, the topographic features further increased in size to 3–5 microns, compared to the sample heated to 400 °C (Fig. 3f). Significant compositional changes of oxygen and

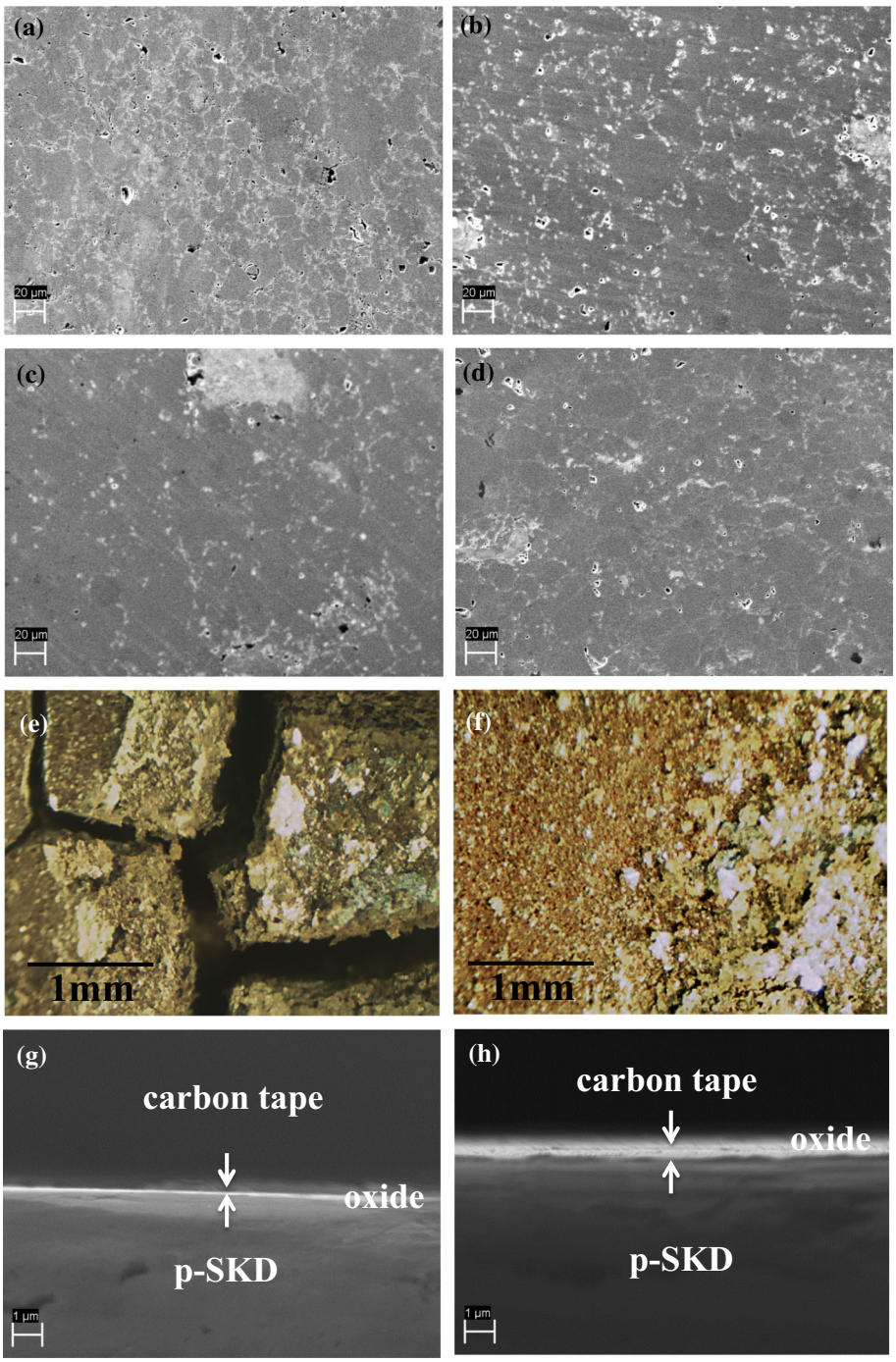

Fig. 5 SEM analysis of p-type $Ce_{0.9}Co_{0.5}Fe_{3.5}Sb_{12}$ after 1 h in air: **a** RT, *top-view*, **b** 100 °C, *top-view*, **c** 200 °C, *top-view*, **d** 300 °C, *top-view*, **e** 400 °C, *top-view*, **f** 500 °C, *top-view*, **g** 100 °C, *vertical-view*, and **h** 300 °C, *vertical-view*

antimony were also observed above 300 °C (Fig. 4). The oxygen and antimony concentration of the RT, 100, 200, and 300 °C were similar in that relatively little change in the surface composition was observed. Above 300 °C, EDS analysis indicated the atomic percentage of oxygen increased and that of antimony and cobalt abruptly decreased, which is consistent with the formation of antimony oxide [14]. In cross-sectional SEM analysis (Fig. 3g–h), 0.1 and 1.8 μm thick oxide layers were observed in the 400 and 500 °C samples.

p-SKD stability versus temperature analysis

The p-type SKD surface topography and composition were also analyzed as a function of heating temperature (Figs. 5 and 6). Compared to the n-type, the p-type SKD microstructure was not as homogenous before heating as indicated by the presence of higher levels of porosity (Fig. 5a). Upon heating, the p-type SKD exhibited a greater degree of oxidation compared to the n-type SKD (Fig. 5b–h). The EDS analysis indicates an abrupt increase in oxygen above

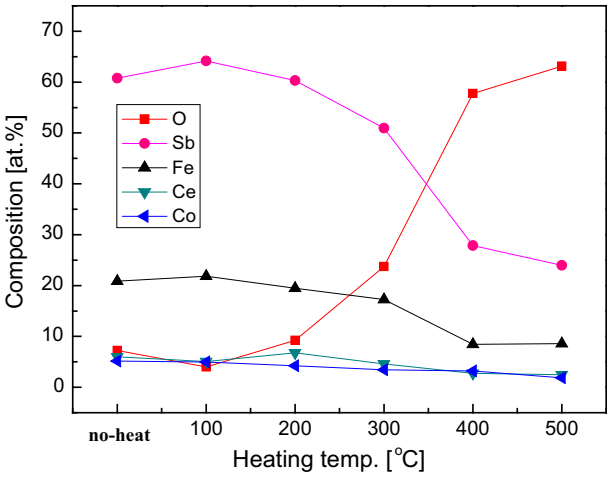

Fig. 6 The element composition changes of p-type $Ce_{0.9}Co_{0.5}Fe_{3.5}Sb_{12}$ after 1 h in air heated at up to 500 °C

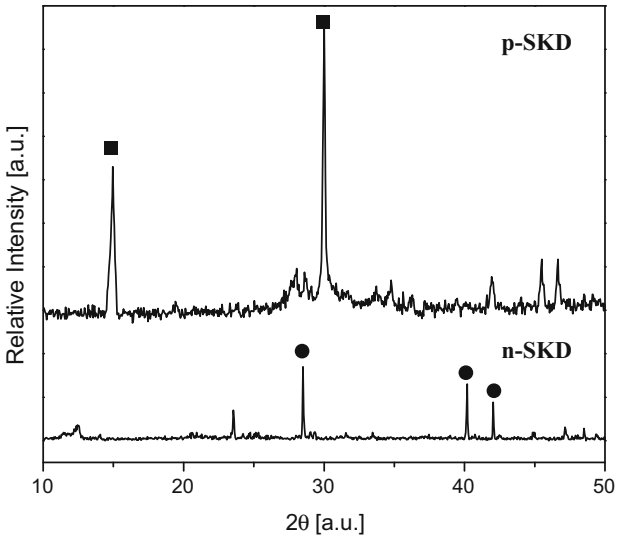

Fig. 7 XRD spectra for n-type $Ba_{0.05}Yb_{0.025}CoSb_3$ and of p-type $Ce_{0.9}Co_{0.5}Fe_{3.5}Sb_{12}$ heated in air at 500 °C for 1 h. The *circles* highlight peaks consistent with Sb_2O_3 ([23] and JCPDS 11-689) and the *squares* highlight peaks consistent with Sb_2O_5 ([24] and JCPDS 33-111)

200 °C (Fig. 6); similar to what was observed in the n-type SKD, but at a lower temperature. The simultaneous decrease in antimony and iron above 200 °C also indicates that the oxide layer may consist of antimony oxide, which is consistent with the observations made by Qiu et al. [16]. Additionally, severe discoloration and cracking occurred at and above 400 °C (Fig. 5e–f). Optical microscopy was used to characterize the surface topography for the samples heated to 400 °C that are shown in Fig. 5e and f, because the features were too large for analysis using SEM. Relatively large (100 μm) cracks occurred in the 400 and 500 °C p-type SKD samples. Compared with the n-type, the p-type samples were more air sensitive, as surmised by the severely cracked and deformed surfaces above 400 and 500 °C. In cross-sectional analysis, 0.1, 0.4, and 0.8 μm thick surface oxide coatings were observed after heating to 100, 200, and 300 °C (Table 1). Thus, it is apparent that the oxide layer grew faster in the p-type compared to the n-type SKD for the same given temperature. The oxidation of SKD is governed by an oxygen-diffusion-limited mechanism [17–19]. Additionally, our results are in good agreement with related work by Chen et al. [20, 21], where the oxidation of p-SKD ($CeFe_4Sb_{12}$) was observed to readily oxidize above 200 °C and the n-SKD ($Yb_yCo_4Sb_{12}$) oxidized above 300 °C.

The Pilling–Bedworth relationship (R_{PB}) determines the ratio between the volumes of an oxide coating grown on a metallic substrate from which the oxide is grown. The R_{PB} can be used to characterize the oxidation behavior of the n- and p-type SKD in this work [22]. R_{PB} is expressed as follow

$$R_{PB} = \frac{V_{antimonyoxide}}{V_{SKD}} = \frac{M_{antimonyoxide} \times \rho_{SKD}}{M_{SKD} \times \rho_{antimonyoxide} \times n}, \quad (2)$$

where $V_{\text{antimony oxide}}$ is the molar volume of antimony oxide, V_{SKD} is the molar volume of SKD, $M_{\text{antimony oxide}}$ is the molecular mass of antimony oxide, M_{SKD} is the molecular mass of SKD, $\rho_{\text{antimony oxide}}$ is the density of antimony oxide, ρ_{SKD} is the density of SKD, and n is the number of SKD atoms per formula unit of antimony oxide, respectively.

Table 2 The physical properties of the enamel at various temperatures. D, ρ, α_{linear}, C_p, and κ are thermal diffusivity, density, linear CTE, specific heat, and thermal conductivity, respectively

T (°C)	50	100	150	200	250	300	350	400	450	500
D (mm^2/sec)	0.59	0.58	0.56	0.54	0.53	–	–	–	–	–
ρ (g/cm^3)	2.55	2.55	2.55	2.55	2.55	2.55	2.55	2.55	2.55	2.54
α_{linear} (ppm/K)	6.7	6.8	7.0	7.1	7.6	7.8	8.0	8.4	8.6	8.9
C_p (J/g K)	0.619	0.660	0.727	0.782	0.820	0.852	0.885	–	–	–
κ (W/m·K)	0.93	0.98	1.04	1.08	1.11	–	–	–	–	–

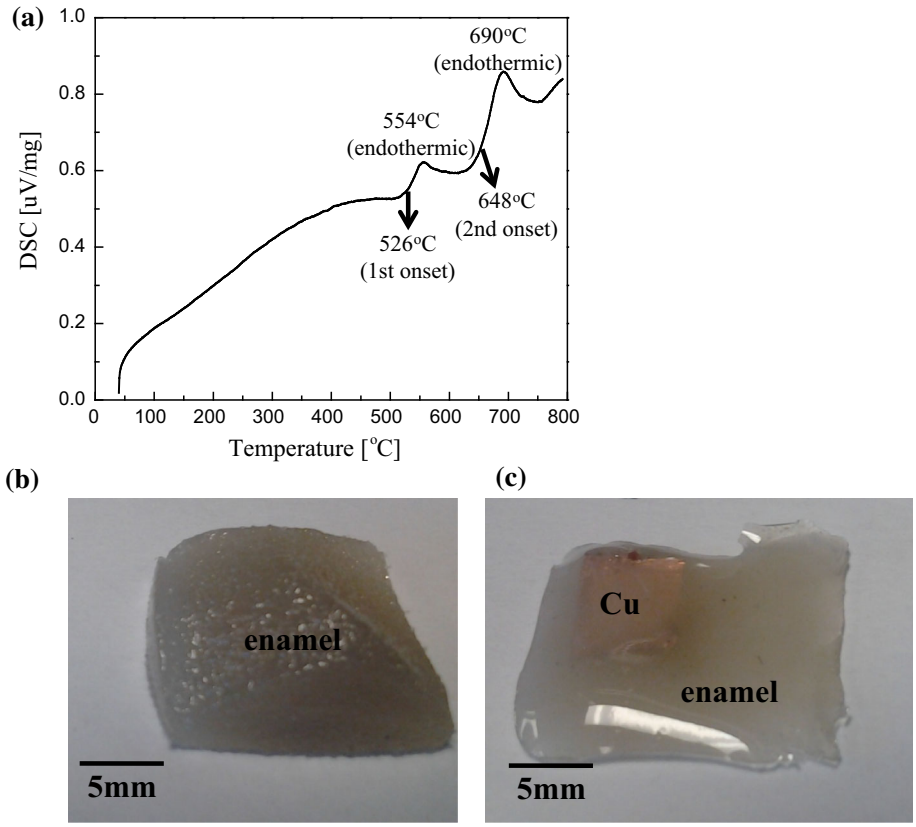

Fig. 8 **a** Enamel DSC analysis, **b** enamel flow test on a Cu coupon at 650 °C in argon, and **c** enamel flow test on a Cu coupon at 700 °C in argon

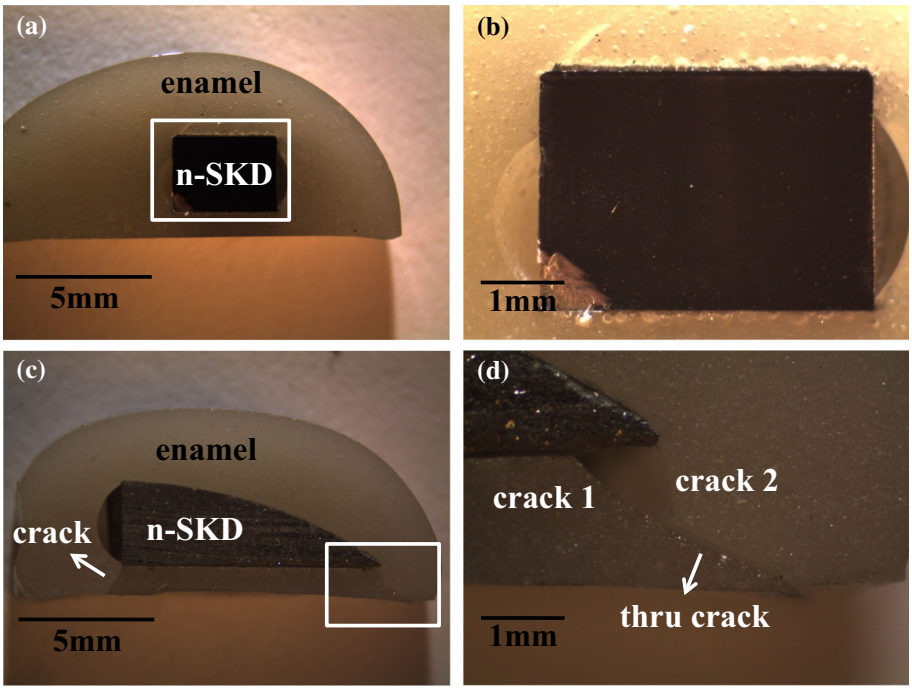

Fig. 9 Effect of chamfering of n-type $Ba_{0.05}Yb_{0.025}CoSb_3$: **a** chamfered orthogonal edge, low magnification, **b** chamfered orthogonal edge (*magnified view*), **c** acute angle edge, low magnification, and **d** acute angle edge (*magnified view*)

To obtain the R_{PB}, the antimony oxide species was identified by XRD analysis. Figure 7 shows that the n-SKD and p-SKD heated in air formed antimony trioxide (Sb_2O_3) and antimony pentoxide (Sb_2O_5), respectively. These observations are consistent with those made by Zhang et al, and Ozawa et al. [24]. M_{Sb2O3} and ρ_{Sb2O3} are 291.52 g/

mole and 5.58 g/cm^3, respectively [25]. M_{Sb2O5} and ρ_{Sb2O5} are 323.52 g/mole and 3.80 g/cm^3, respectively [26]. $M_{n\text{-}SKD}$ and $M_{p\text{-}SKD}$ were determined to be 435.41 and 1812.15 g/mole, respectively. $\rho_{n\text{-}SKD}$ and $\rho_{p\text{-}SKD}$ were determined to be 7.63 and 7.60 g/cm^3 at room temperature, respectively. For the $R_{PB\text{-}n\text{-}SKD}$ calculation, we assumed the number of antimony atoms in the SKD was equivalent to the antimony atom in SKD formula. Thus, the n values are 2/3 in n-SKD and 2/12 in p-SKD, respectively. In the case of n-SKD, the $R_{PB\text{-}n\text{-}SKD}$ was 1.37, which is in the protective R_{PB} range ($1 < R_{PB} < 2$). Thus, the antimony oxide provided somewhat of a protective barrier against further surface oxidation for the n-SKD compared to the p-type. However, in the case of p-SKD, the $R_{PB\text{-}p\text{-}SKD}$ was 2.14, which is in the non-protective range ($R_{PB} < 1$ or $R_{PB} > 2$). The relatively larger $R_{PB\text{-}p\text{-}SKD}$ indicates the oxide volume is larger in the p-type compared to the n-type SKD likely causing cracking and spallation.

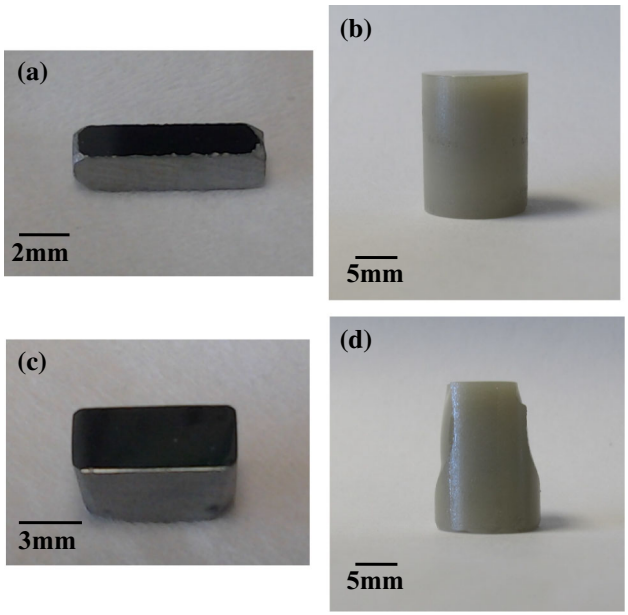

Fig. 10 Enamel coating on n-type $Ba_{0.05}Yb_{0.025}CoSb_3$ or p-type $Ce_{0.9}Co_{0.5}Fe_{3.5}Sb_{12}$. **a** Chamfered n-SKD, before coating, **b** chamfered n-SKD, after coating, **c** chamfered p-SKD, before coating, and **d** chamfered p-SKD, after coating

Enamel physical property characterization

The physical properties of the enamel were measured and are summarized in Table 2. The thermal conductivity is 0.93 W/m K at 50 °C, which is approximately 10 times

Table 3 Efficacy testing of enamel-coated n- and p-SKD under various conditions

	T (°C)	SKD type	Time interval	SEM and EDS results after test
Isothermal	500	n	8 continuous days	1) No surface oxide dlx 2) No oxygen and antimony composition change with depth in a sample
		p		
	600	n		
		p		
Cycling	600	n	20 cycles	
		p		

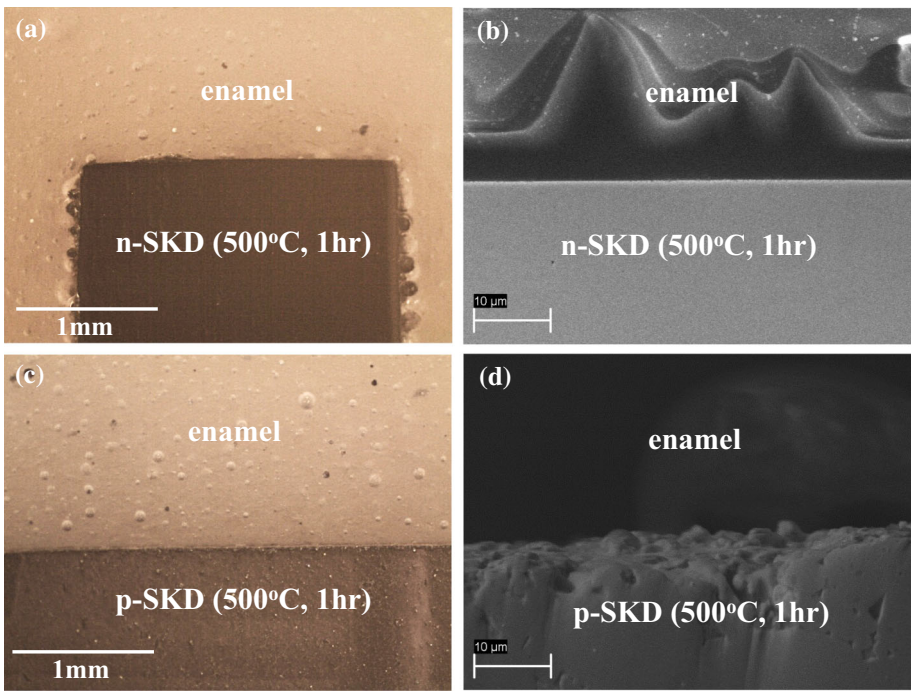

Fig. 11 OM and SEM analysis after 500 °C 1 h air test. Enamel-coated and chamfered n-type $Ba_{0.05}Yb_{0.025}CoSb_3$: **a** OM, **b** SEM. Enamel-coated and chamfered p-type $Ce_{0.9}Co_{0.5}Fe_{3.5}Sb_{12}$: **c** OM, **d** SEM

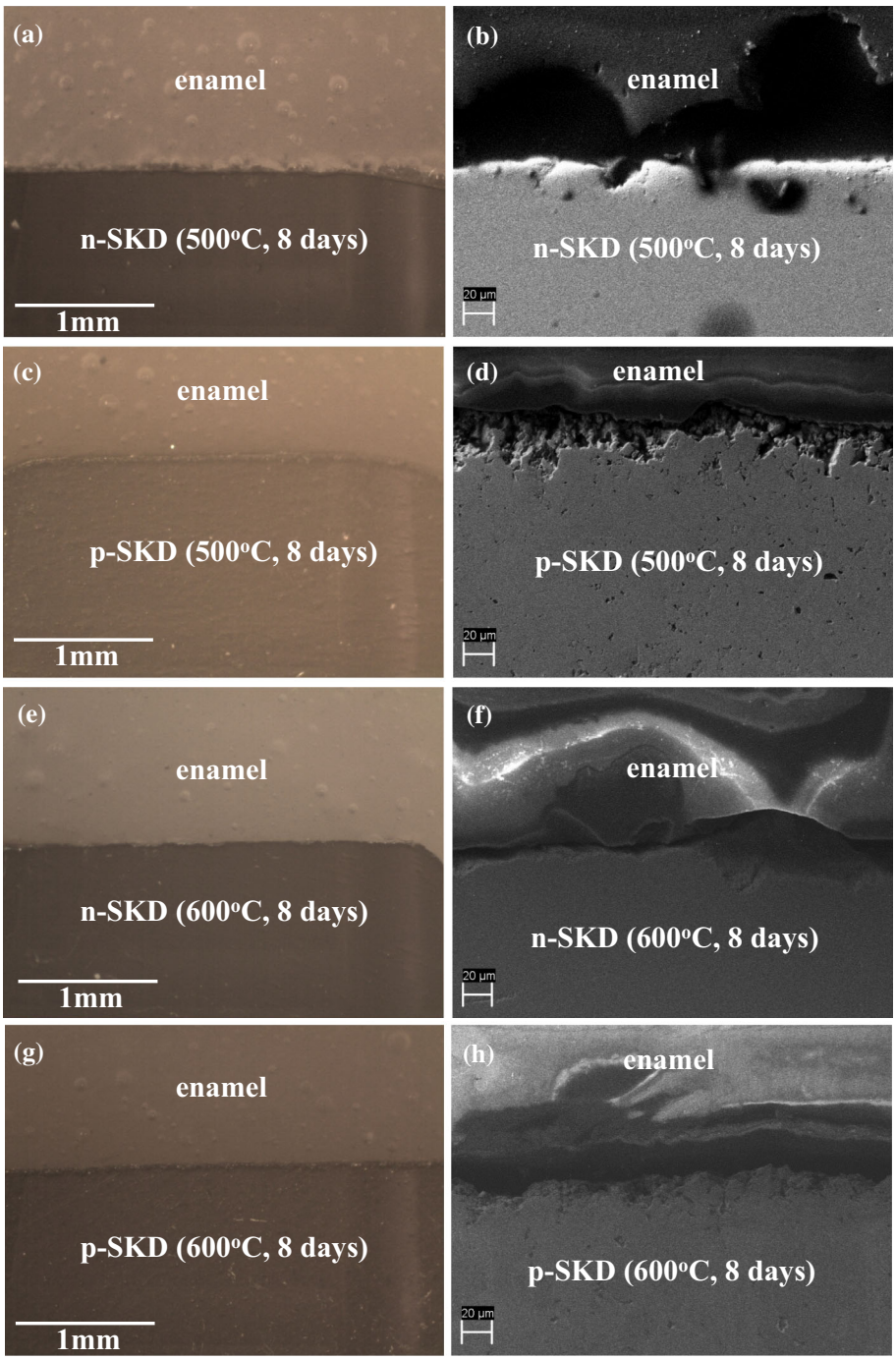

Fig. 12 OM and SEM analysis of enamel-coated SKD. n-SKD heated at 500 °C for 8 days: **a** OM, **b** SEM. p-SKD heated at 500 °C for 8 days: **c** OM, **d** SEM. n-SKD heated at 600 °C for 8 days: **e** OM, **f** SEM. p-SKD heated at 600 °C for 8 days: **g** OM, **h** SEM. n-SKD heated between 600 °C and room temperature for 20 cycles: **i** OM, **j** SEM. p-SKD heated between 600 °C and room temperature for 20 cycles: **k** OM, **l** SEM

lower than the n-type $CoSb_3$ and six times lower than the p-type $CeFe_3CoSb_{12}$ [4, 27–29].

Assuming a 0.1 mm thick enamel coating on 3.5 mm × 3.5 mm square cross section SKD leg that is 6 mm long (dimensions used in previous SKD generator prototype generators [8]), the parasitic heat loss through can be estimated using the following relationships.

$$U = \kappa \frac{A}{L} \tag{3}$$

$$\frac{U_{enamel}}{U_{SKD}} = \frac{\kappa_{enamel} \times A_{enamel}}{\kappa_{SKD} \times A_{SKD}} = \frac{\kappa_{enamel}}{\kappa_{SKD}} \times \frac{(3.7^2 - 3.5^2)}{3.5^2} \tag{4}$$

$$\frac{U_{enamel}}{U_{n-SKD}} = \frac{1}{10} \times \frac{(3.7^2 - 3.5^2)}{3.5^2} = 0.01, \tag{5}$$

Fig. 12 continued

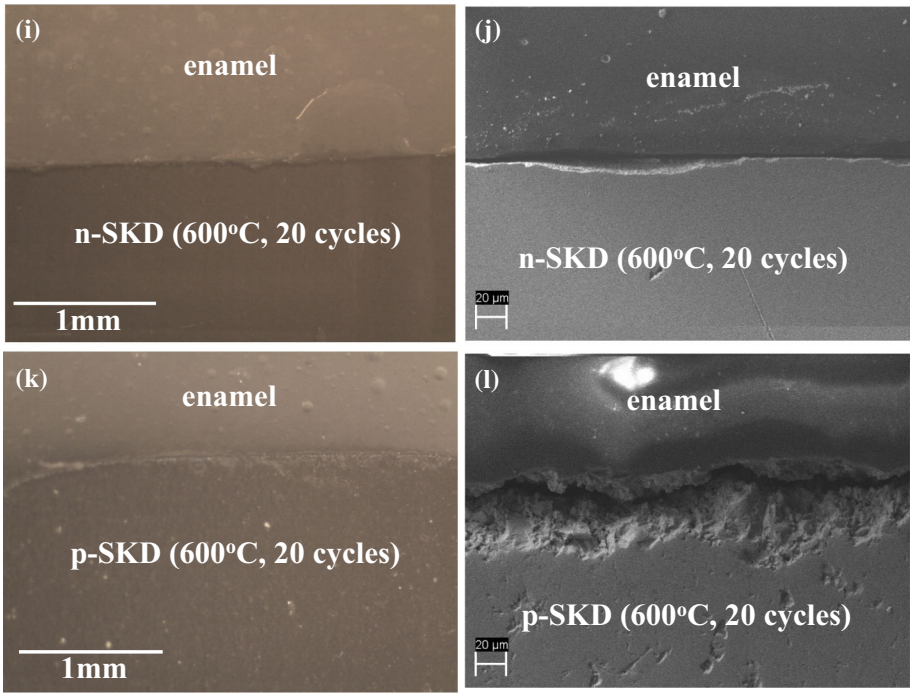

$$\frac{U_{enamel}}{U_{p-SKD}} = \frac{1}{6} \times \frac{(3.7^2 - 3.5^2)}{3.5^2} = 0.02, \quad (6)$$

where U is the thermal conductance, A is area, and L is length. Based on these calculations the parasitic heat loss is 1 and 2 percent of the total thermal conductance for the n- and p-type SKD elements. These calculations confirm that the impact on device efficiency will likely be low. Further work is required to determine how thin the enamel coatings can be made and still provide adequate oxidation protection to better estimate the parasitic heat loss.

The CTE was measured using dilatometery and was determined to be 6.7 ppm/K at 50 °C, which is approximately 6.8 and 6.0 ppm/K lower (or about 100 % lower) than the n- and p-type SKD, respectively [27]. This mismatch in the CTE could be advantageous in that the coating will be under compressive stress during operation. This approach is analogous to tempering glass to suppress surface crack propagation [30].

DSC analysis was conducted to determine the enamel melting or flowing temperature. It was determined that the two endothermic reactions at 526 and 648 °C could be attributed to melting (Fig. 8a). It is possible that an inhomogeneous distribution of constituents could explain the observation of two melting temperatures.

Melting and flowing behavior was characterized by melting enamel on copper samples. This particular enamel composition is known to be compatible with Cu, thus it served as a control to demonstrate that the enamel could adhere to a metallic component with dimension comparable to a thermoelectric element. At 650 °C, the enamel did not sufficiently flow as indicated by the relatively rough or granular surface (Fig. 8b). However, at 700 °C, the enamel flowed sufficiently to provide a uniform, transparent coating around the copper sample (Fig. 8c). Thus, 700 °C was used to flow enamel around SKD samples.

Enamel coating

In the initial tests with SKD, the enamel coatings cracked upon heating. We, therefore, chamfered the SKD coupon edges to reduce stresses and, therefore, cracking. Characterizing the efficacy of the chamfering was studied by comparing n-SKD samples with chamfered and square edges (Fig. 9). After the initial enameling process, both samples had crack-free coatings. However, after heating both samples at 500 °C for 1 h in air, the enamel coating on the chamfered sample was not cracked, while the enamel coating on the sample with square edges was (Fig. 9c–d). It is apparent that cracks are mainly generated at sharp corners where stresses are concentrated. Several chamfered and non-chamfered SKD samples were coated with enamel. In general, the enamel coatings on the non-chamfered samples cracked, while no cracking was observed on the chamfered samples.

After the enamel coating process (heat to 700 °C in argon), the n-type $Ba_{0.05}Yb_{0.025}CoSb_3$ and the p-type $Ce_{0.9}Co_{0.5}Fe_{3.5}Sb_{12}$ were successfully coated as shown in

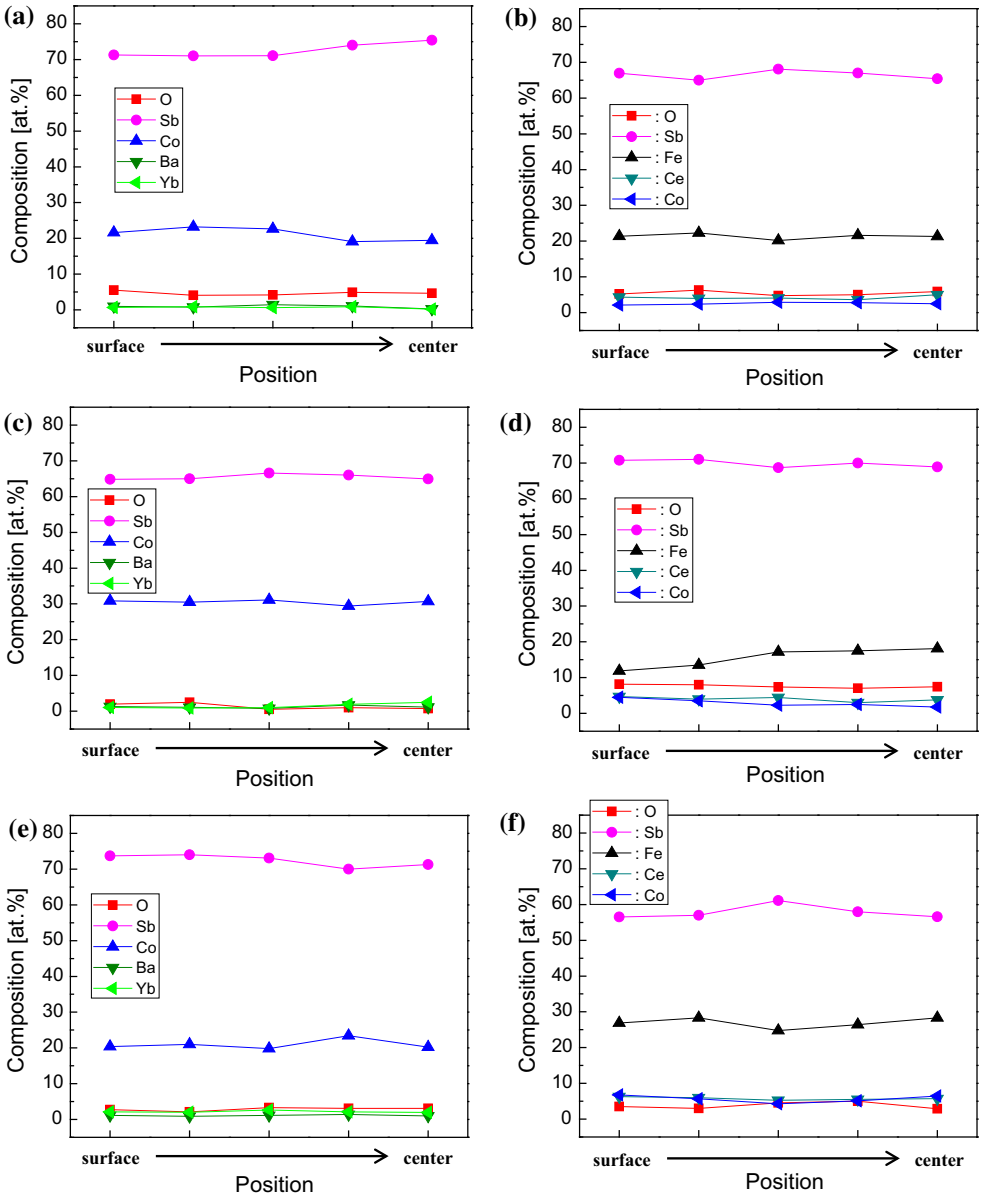

Fig. 13 The element composition as a function of position across the enamel-SKD interface after the thermal stability air test. **a** n-SKD heated at 500 °C for 8 days, **b** p-SKD heated at 500 °C for 8 days, **c** n-SKD heated at 600 °C for 8 days, **d** p-SKD heated at 600 °C for 8 days, **e** n-SKD heated between 600 °C and room temperature for 20 cycles, and **f** p-SKD heated between 600 °C and room temperature for 20 cycles

Fig. 10. The ratio of grams of enamel to grams of SKD was approximately 1. The appearance of the enamel-coated SKD samples was similar to the previous experiments using copper samples in that a uniform enamel coating formed.

Enamel coating efficacy testing (short term −1 h at 500 °C)

To characterize the high temperature stability of enamel-coated SKD samples, they were heated in air at 500 °C for 1 h. There were no appreciable changes after the oxidation test. After testing, the samples were cross-sectioned and characterized using OM and SEM (Fig. 11). No significant signs of n- or p-type SKD oxidation were observed. We believe this is the first report demonstrating an enamel coating that can suppress oxidation in air at 500 °C for both n- and p-type SKD.

Enamel coating efficacy testing (longer-term thermal annealing at 500 and 600 °C for 8 days, and 20 cycle tests between 600 °C and room temperature)

Table 3 shows the isothermal and thermal cycle test results of the enamel protected n- and p-type SKD samples. Figure 12 shows that no surface oxide was observed in the extended isothermal and thermal cycle tests. Some lines and dots in the enamel near the SKD surface (Figs. 11 and

12) are due to charging effects. EDS analyses indicated that oxygen and antimony concentrations at the surfaces were similar with those in the center of the samples as shown in Fig. 13. In addition, the oxygen concentrations closely matched with un-heated SKD samples (Figs. 4 and 6). The results indicate that the enamel coating is effective in preventing oxidation of SKD at 500 and 600 °C in air. Although the p-SKD-enamel interface appears to have reacted more than the n-SKD-enamel interface, the coating remained intact over the 8 days of continuous heating and 20 cycles between room temperature and 600 °C. Evaluating the longer-term stability over hundreds of thermal cycles and weeks of isothermal testing is still on-going. Additionally, although the heating and cooling rates are likely lower than what would be expected in a Federal Standard Test (FTP) cycle, these preliminary data suggest that despite the difference in CTE, the enamel coatings remained intact throughout the 20 cycle test.

Summary

This work demonstrated the efficacy of enamel coatings to suppress oxidation of n-type $Ba_{0.05}Yb_{0.025}CoSb_3$ and p-type $Ce_{0.9}Co_{0.5}Fe_{3.5}Sb_{12}$ SKD. This is the first report demonstrating the efficacy of enamel coatings to suppress oxidation in p-SKD containing oxygen-sensitive elements such as Ce, La, Fe, and Sb. Enamel coatings prevented oxidation of n- and p-type SKD when tested up to 600 °C in air continuously for 8 days or thermally cycled for 20 cycles. It was also determined that chamfering SKD elements was necessary to lower stressed at the edges and prevent cracking of the enamel coating. The enamel physical and processing properties were also characterized and were determined to be compatible with SKD-based technology fabrication and operation conditions.

Acknowledgements The authors would like to acknowledge support from General Motors and the Department of Energy, Energy Efficiency, and Renewable Energy under Award Number DE-EE0005432.

References

1. Tritt TM, Subramanian MA (2006) Thermoelectric materials, phenomena, and applications: a bird's eye view. MRS Bull 31:188–198
2. Snyder GJ, Toberer ES (2008) Complex thermoelectric materials. Nat Mater 7:105–114
3. Uher C (2006) Skuttetudite-based thermoelectrics. In: Rowe DM (ed) Thermoelectrics handbook: macro to nano. CRC Press, Boca Raton, Chapter 34, pp 1–17
4. Nolas GS, Morelli DT, Tritt TM (1999) Skutterudites: a phonon-glass-electron crystal approach to advanced thermoelectric energy conversion applications. Annu Rev Mater Sci 29:89–116
5. Sales BC, Mandrus D, Williams BK (1996) Filled skutterudite antimonides: a new class of thermoelectric materials. Science 272:1325–1328
6. Shi X, Yang J, Salvador JR, Chi M, Cho JY, Wang H, Bai S, Yang J, Zhang W, Chen L (2011) Multiple-filled skutterudites: high thermoelectric figure of merit through separately optimizing electrical and thermal transports. J Am Chem Soc 133:7837–7846
7. Salvador JR, Cho JY, Ye Z, Moczygemba JE, Thompson AJ, Sharp JW, Konig JD, Maloney R, Thompson T, Sakamoto J, Wang H, Wereszczak AA, Meisner GP (2013) Thermal to electrical energy conversion of skutterudite-based thermoelectric modules. J Electron Mater 42:1389–1399
8. Sakamoto JS, Schock H, Caillat T, Fleurial J-P, Maloney R, Lyle M, Ruckle T, Timm E, Zhang L (2011) Skutterudite-based thermoelectric technology for waste heat recovery: progress towards a 1 kW generator. Sci Adv Mater 3:1–12
9. Yang J, Stabler FR (2009) Automotive application of thermoelectric materials. J Electron Mater 38:1245–1251
10. Li H, Tang X, Zhang Q, Uher C (2009) High performance $In_xCe_yCo_4Sb_{12}$ thermoelectric materials with in situ forming nanostructured InSb phase. Appl Phys Lett 94:102114
11. Melnyk G, Bauer E, Rogl P, Skolozdra R, Seidl E (2000) Thermoelectric properties of ternary transition metal antimonides. J Alloy Compd 296:235–242
12. Garcia-Canadas J, Powell AV, Kaltzoglou A, Vaqueiro P, Min G (2013) Fabrication and evaluation of a skutterudite-based thermoelectric module for high-temperature applications. J Electron Mater 42:1369–1374
13. Zawadzka K, Godlewska E, Mars K, Nocun M (2011) Oxidation resistant coating for CoSb3, 9th European Conference on Thermoelectrics B_25_P
14. Dong H, Li X, Huang X, Zhou Y, Jiang W, Chen L (2013) Improved oxidation resistance of thermoelectric skutterudites coated with composite glass. Ceram Int 39:4551–4557
15. Sakamoto JS, Snyder G, Calliat T, Fleurial J-P, Jones SM, Paik J-A (2006) System and method for suppressing sublimation using opacified aerogel. US Patent application no. 20060090475 A1, May 04 2006
16. Qiu P, Xia X, Huang X, Gu M, Qiu Y, Chen L (2014) Pesting-like oxidation phenomenon of p-type filled skutterudite $Ce_{0.9}Fe_3CoSb_{12}$. J Alloy Compd 612:365–371
17. Hara R, Inoue S, Kaibe HT, Sano S (2003) Aging effects of large-size n-type $CoSb_3$ prepared by spark plasma sintering. J Alloy Compd 349:297–301
18. Godlewska E, Zawadzka K, Adamczyk A, Mitoraj M, Mars K (2010) Degradation of $CoSb_3$ in air at elevated temperatures. Oxid Met 74:113–124
19. Leszczynski J, Wojciechowski KT, Malecki AL (2011) Studies on thermal decomposition and oxidation of $CoSb_3$. J Therm Anal Calorim 105:211–222
20. Xia X, Qiu P, Shi X, Li X, Huang X, Chen L (2012) High-temperature oxidation behavior of filled skutterudites $Yb_yCo_4Sb_{12}$. J Electron Mater 41:2225–2231
21. Xia X, Qiu P, Huang X, Wan S, Qui Y, Li X (2014) Chen L (2014) Oxidation behavior of filled skutterudite $CeFe_4Sb_{12}$ in air. J Electron Mater 43:1639–1644
22. Pilling NB, Bedworth RE (1923) The oxidation of metals in high temperature. J Inst Met 29:529–591
23. Zhang Y, Li G, Zhang J, Zhang L (2004) Shape-controlled growth of one-dimensional Sb_2O_3 nanomaterials. Nanotechnology 15:762–765
24. Ozawa K, Sakka Y, Amano M (1998) Preparation and electrical conductivity of three types of antimonic acid films. J Mater Res 13:830–833
25. Svensson C (1975) Refinement of the crystal structure of cubic antimony trioxide Sb_2O_3. Acta Crystallogr A B31:2016–2018

26. Eagleson M (1994) Concise encyclopedia chemistry. Walter De Gruyter, Germany, p 18
27. Rogl G, Zhang L, Rogl P, Grytsiv A, Falmbigl M, Rajs D, Kriegisch M, Muller H, Bauer E, Koppensteiner J, Schranz W, Zehetbauer M, Henkie Z, Maple MB (2010) Thermal expansion of skutterudites. J Appl Physics 107:043507
28. Tang XF, Chen LD, Goto T, Hirai T, Yuan RZ (2001) Synthesis and thermoelectric properties of filled skutterudite compounds $Ce_yFe_xCo_{4-x}Sb_{12}$ by solid state reaction. J Mater Sci 36:5435–5439. doi:10.1023/A:1012473428845
29. Chubilleau C, Lenoir B, Masschelein P, Dauscher A, Candolfi C, Guilmeau E, Godart C (2013) High temperature thermoelectric properties of $CoSb_3$ skutterudites with PbTe inclusions. J Mater Sci 48:2761–2766. doi:10.1007/s10853-012-6891-3
30. Richardson RE (1961) Blowing frame for tempering glass sheets. US Patent no. 2968126, January 17 1961